

Sintering characteristics of nanocrystalline TiO₂—A study combining small angle neutron scattering and nitrogen absorption—BET

W. Wagner

Paul Scherrer Institute, CH-5232 Villigen, PSI, Switzerland

R. S. Averback and H. Hahn^{a)}

Department of Materials Science and Engineering and Materials Research Laboratory, University of Illinois at Urbana–Champaign, 1304 West Green Street, Urbana, Illinois 61801

W. Petry

Institute Laue Langevin, 156X, F-38042, Grenoble, France

A. Wiedenmann

Hahn Meitner Institute, Glienicker Str. 100, D-1000, Berlin 39, Germany

(Received 11 February 1991; accepted 4 June 1991)

Small angle neutron scattering (SANS) was employed to characterize the pore structure of nanophase TiO₂ ceramic materials compacted at different temperatures. Nanophase samples, produced by inert gas condensation, were compacted at 25, 290, 413, and 550 °C using a pressure of ≈ 1 GPa. The pore size distribution of the sample compacted at room temperature was very broad, with sizes ranging from ≈ 3 –30 nm and pores comprising 38% of the sample volume. Compaction at 290 and 413 °C reduced the pore volume to 25% and 20%, respectively, by eliminating pores at both the small and large ends of the distribution. Compaction at 550 °C resulted in a pore volume that was less than 8%. Complications in the SANS analysis arising from the scattering from grain boundaries are discussed. The results from SANS are compared with those derived from nitrogen absorption, BET, measurements.

I. INTRODUCTION

The structures of nanophase materials are unique since grain boundaries comprise a significant fraction of the total volume of the material. It is not surprising, therefore, that the properties of nanophase materials are often very different from those of their counterpart polycrystalline materials having larger grain sizes. In nanophase ceramics, sinterability and mechanical properties are of particular interest since it has been reported that densification, diffusional creep, and superplastic behavior are possible at low temperatures.^{1–4} Small grain sizes, however, are not the only important microstructural features in nanophase ceramics that have a strong influence on mechanical properties; flaws, such as residual porosity, also affect these properties.⁵ We have previously studied the microstructure of nanophase (*n*–) TiO₂ during sintering using a variety of techniques: gravimetry (using Archimede's principle), BET nitrogen absorption, scanning electron microscopy, and x-ray diffraction.⁶ Although this investigation provided an overview of the microstructural development in *n*–TiO₂ during sintering, a detailed understanding of the pore structure and its evolution in nanophase ceramics is

still lacking. This work was initiated to evaluate the efficacy of small angle neutron scattering (SANS) for this purpose as well as to characterize better the structure of these materials. In polycrystalline samples with larger grain sizes, SANS has proved to be a powerful technique for quantitatively determining the distribution of void or precipitate sizes and for following the kinetics of their evolution.⁷ Nanocrystalline materials, however, pose special problems for SANS since the length scale of the microstructural fluctuations that give rise to scattering from pores is approximately the same as that from the grain boundaries, preventing unambiguous determination of either distribution. In this study, BET, x-ray diffraction, and gravimetry were used to complement the SANS measurements to test how well the pore size distribution could be specified.

II. EXPERIMENTAL PROCEDURES

The samples employed for these experiments were produced using a three-step process; this has been described elsewhere.^{4,6,8} Since the microstructures of our samples are very sensitive to the way that they are prepared, we outline here the more cogent aspects of this process. First, Ti particles are produced by vaporizing Ti metal from a resistive W boat into an ambient helium atmosphere at a pressure of 2 mbar. This method, i.e.,

^{a)}Now at Rutgers, The State University of New Jersey, Piscataway, New Jersey 08855.

inert gas condensation, yields Ti particles that have a diameter of ≈ 10 nm. The particles are carried in the He convection current to a cold shroud, where they loosely adhere. The He gas is then removed from the chamber and replaced with O₂ gas. The Ti particles undergo rapid oxidation and usually glow red, indicating that they momentarily reach temperatures over ≈ 800 °C. The powder is nearly fully oxidized during this “burning” with the average composition becoming TiO_{1.8}.⁶ Since the powder is sparsely distributed over the cold shroud, agglomeration is limited. The oxidized powders are subsequently removed from the cold shroud and collected, *in vacua*, in a powder press where they are lightly compacted and further oxidized at 350 °C in a partial pressure of O₂ of ≈ 300 mbar. In the final step of the process, the samples are highly compacted using the same oxygen ambient but under an applied pressure of ≈ 1.0 GPa at the specified temperature. It was shown previously^{1,6} that the density of the unsintered compacted powder depends strongly on the compaction temperature in the temperature range 25–550 °C, but that the grain size does not. Accordingly, specimens were produced at different compaction temperatures to provide samples of similar grain size but different volume fractions of porosity. Table I lists the preparation conditions and the physical characteristics of the samples.

The samples were characterized using gravimetry, BET, x-ray diffraction, and SANS. The x-ray diffraction patterns indicated that all of the samples had the rutile structure, which is the equilibrium phase of TiO₂. The relative densities of the samples are listed in Table I; they derive from BET or gravimetry measurements, depending on whether they had open or closed porosity (samples A and B were assumed to have open porosity; sample D was known, from BET, to have closed porosity; and sample C was assumed to have a mixture of open and closed porosity, and therefore its density was obtained from an average of the two methods. These values will be compared with the SANS results and evaluated below.

III. BET RESULTS

The BET results for the pore size distributions are shown in Fig. 1, where the incremental pore volume

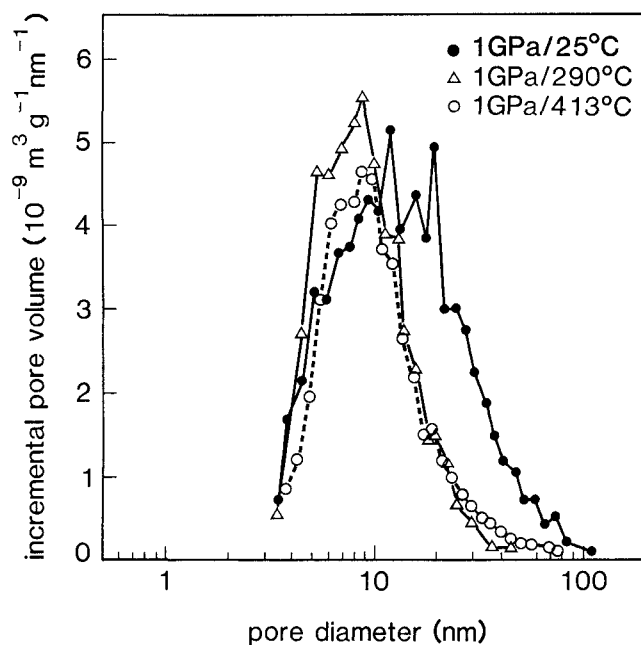


FIG. 1. Pore size distribution in nanocrystalline TiO₂ after compaction at different temperatures as determined by BET.

is plotted as a function of pore diameter. The sample compacted at 550 °C is not shown as no open porosity was detectable. The pore-size distribution of the sample compacted at 25 °C shows features similar to those reported earlier,⁶ a rather broad distribution of sizes with the full width at half maximum extending from ≈ 4 to 30 nm. The distribution changes significantly when the compaction is performed at 290 °C rather than at room temperature. The fractional pore volume is reduced from 0.38 to 0.25, and a substantial reduction in the number of large pores is observed. When the compaction temperature is raised further, to 413 °C, the additional changes are rather small; the pore volume is reduced an additional $\approx 5\%$, with this reduction occurring at the expense of the smaller pores.

IV. SMALL ANGLE NEUTRON SCATTERING

The SANS measurements were carried out at the D11-instrument of the Institute Laue Langevin, Grenoble, France.⁹ The neutron wavelength, λ , was 0.70 nm and the specimen-to-detector distance was 1.2, 7.0,

TABLE I. Physical characteristics of the nanocrystalline TiO₂ samples.

Specimen	Preparation			Macroscopic density, ρ/ρ_0	Grain (nm)	Thickness (mm)	BET density
	Temp.	Pressure	Time				
A	RT	1.05 GPa	1.25 h	0.62	14.8	0.561	62%
B	290 °C	1.05 GPa	18 h	0.75	11.5	0.268	75%
C	413 °C	1.05 GPa	5.5 h	0.80	10.6	0.218	76%
D	550 °C	1.05 GPa	7 h	0.92	12.5	0.240	Dense

and 35 m, covering a range in momentum transfer, Q , of $1.3 \times 10^{-2} < Q/\text{nm}^{-1} < 2.5$. $Q = (4\pi/\lambda) \sin \theta/2$, where θ is the scattering angle. All measurements were performed at room temperature, with the specimen in air, mounted behind a circular Cd aperture of 3 mm diameter.

The intensity data were corrected for background scattering, transmission factors, and specimen geometry. Variations in the acceptance of different elements of the area sensitive detector were corrected by normalizing to a water spectrum. The two-dimensional data did not show radial anisotropy around the central beam, and therefore it was averaged for equal radial positions of the detector. Absolute values of the differential scattering cross section, $d\sigma(Q)/d\Omega$, in units of barn/sr per TiO₂-molecule were determined by referring to the averaged incoherent scattering of a water specimen.

The SANS scattering intensities for the specimen compacted at room temperature and for those compacted at higher temperatures are plotted in Fig. 2 as a function of scattering vector, Q . Double logarithmic scales are employed since the data extend over several decades. Compared to the specimen compacted at 25 °C, the scattering from samples compacted at elevated temperatures, which have many fewer pores, is significantly reduced, showing that a large contribution of the SANS scattering does, indeed, derive from pores. The SANS data for the sample compacted at 413 °C are found almost coincident with the data for the sample compacted at 290 °C. It seems that this difference in compaction temperature did not yield an appreciable difference in the pore microstructure. This is consistent with the BET data.

After sintering at 1 GPa and 550 °C, the measured SANS intensity is lowest. The BET measurements indicate that no open porosity remained after this treatment. In addition, the macroscopic density of 92%, relative to bulk rutile, suggests that most of the porosity has been removed from this specimen. However, what fraction of the 8% excess volume is due to residual closed porosity, and what fraction to grain boundaries, cannot be determined from our measurements. Nevertheless, as a working hypothesis, the SANS scattering from this specimen was assumed to originate totally from structural inhomogeneities of the nanoscale material, i.e., grains, grain boundaries, and surface roughness; accordingly, the scattering from this sample was taken as a reference for subtracting the scattering contribution from those same sources in the other specimens. Although the assumption that the reference sample is free of porosity cannot be fully justified from the measurements, it should be noted that the SANS intensity derived from this sample, and used for subtraction, comprises only a small fraction of the intensity attributed to pores in the other samples.

SANS data evaluation

A quantitative evaluation of the SANS data was carried out using the standard procedure of calculating $d\sigma(Q)/d\Omega$, on the basis of a modeled microstructure. Our model included contributions from the following scattering structures:

(i) Large heterogeneities ($d > 500$ nm), e.g., surface roughness or internal macroscopic structures. These are characterized by a Q^{-4} -dependent scattering at small Q , as described by Porod's law

$$d\sigma_0(Q)/d\Omega = P \times Q^{-4} \quad (1)$$

where P is the Porod constant. For all of the nanocrystalline specimens in this study, Porod's constant was $P = (0.9 \pm 0.2) \times 10^{-2}$ barn nm⁻⁴. The Porod constant is not of direct interest here, nor does it influence the results; nevertheless, it is included in the SANS model for completeness.

(ii) Grains of bulk rutile TiO₂-material, surrounded by interfacial regions (grain boundaries) of reduced density. This contribution is denoted as $d\sigma_1(Q)/d\Omega$.

(iii) Pores and cavities. This contribution is denoted as $d\sigma_2(Q)/d\Omega$.

Interference effects are neglected in this model (the scattering curves do not show any indication that they are significant), so that the three contributions to the scattering intensity can be treated independently, i.e.,

$$\frac{d\sigma}{d\Omega}(Q) = P \times Q^{-4} + \frac{d\sigma_1}{d\Omega}(Q) + \frac{d\sigma_2}{d\Omega}(Q) \quad (2)$$

For $d\sigma_n(Q)/d\Omega$ ($n = 1, 2$), an ansatz for polydisperse arrays of scattering particles was used

$$\left(\frac{d\sigma_n(Q)}{d\Omega} \right) = \frac{(1-q)^2 (\Delta b)^2}{\Omega} \int_R F^2(Q, R) V(R) N_n(R) dR \quad (3)$$

Ω is the volume occupied by a TiO₂-molecule in bulk rutile ($\Omega = 0.0311$ nm³), and $(\Delta b)^2$ is the average neutron scattering contrast of bulk rutile against vacuum [$(\Delta b)^2 = 0.668$ barn/sr]. The factor $(1-q)^2$ accounts for a finite intermediate density in the interfacial regions; q is the ratio of interfacial to bulk rutile densities. For pores or cavities, $q = 0$.

Generalized for voids and grains, the single particle scattering function $F(Q, R)$ is approximated by the structure function for spheres of radius R ,

$$F(x) + \frac{3}{x^3} (\sin x - x \cos x) \quad (4)$$

with $x = QR$. Deviations from a spherical shape become convoluted with the size distribution and therefore would not significantly disturb the model assumptions. $V(R)$

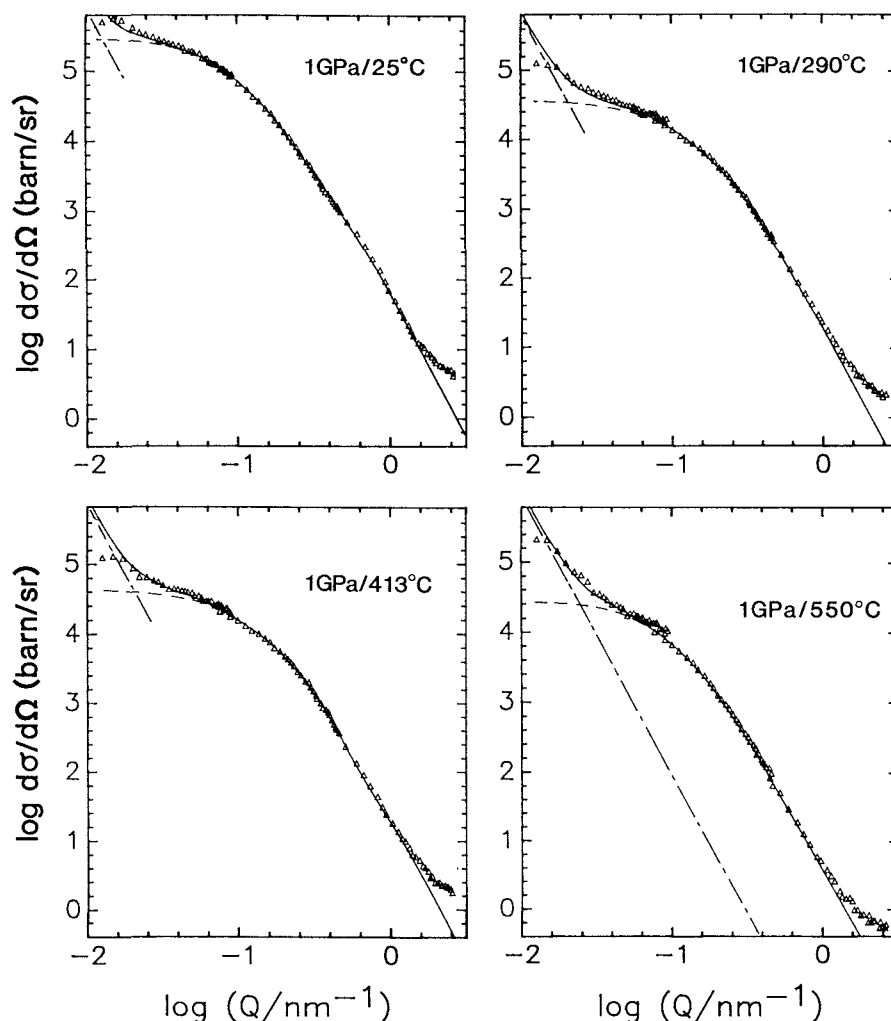


FIG. 2. SANS intensity data of nanocrystalline TiO₂, in units of barn/sr per TiO₂ molecule, after compaction at room temperature and elevated temperatures, as indicated. The solid curves are modeled structure functions fitted to the data. Contributions following Eq. (1) (dash-dotted lines) and Eq. (3) (dashed curves) are separately extrapolated.

is the particle volume, and $N(R)dR$ is the incremental volume fraction of particles in the size interval between R and $R + dR$.

$N(R)$ describes the size distribution of the scattering particles, yielding the average size and average volume. In addition, integration over $N(R)$ yields the total volume fraction of the scattering particles, i.e.,

$$f_p = \int_R N(R) dR \quad (5)$$

The model structure function, Eq. (2), was fit to the data by means of an interactive trial and error procedure, varying the parameter P , and the distribution functions $N(R)$. Attempts to parametrize the $N(R)$ functions revealed that the underlying size distributions of scattering particles were extremely broad. A suitable fit of the data could be obtained using a linear combination of four log-normal functions for $N(R)$, centered at positions R_0 ,

$2R_0$, $4R_0$, and $8R_0$, with all having the same width, σ , but different amplitudes A_k :

$$N(R) = \sum_{k=1}^4 A_k \exp - \frac{\{\log R / (R_0 \times 2^{k-1})\}^2}{2\sigma^2} \quad (6)$$

The best fits for $d\sigma(Q)/d\Omega$ derived from our scattering model are plotted in Fig. 2 as solid curves. The SANS data are shown for comparison. It should be noticed that the model curves describe the measured scattering curves rather well over more than two decades in Q , and over more than four decades in the scattering intensity, $d\sigma(Q)/d\Omega$. The deviations at large Q occur from neglecting the incoherent scattering of TiO₂, $(d\sigma/d\Omega)_{\text{inc}} = 0.235$ barn/sr, and possibly also from incoherent scattering of resorbed hydrogen in the specimens, $(d\sigma/d\Omega)_{\text{inc}} = 12.7$ barn/sr per H₂-molecule. H₂-resorption to an amount of 1–3 at. % has recently been observed in nanocrystalline Ni by phonon density

of states measurements.¹⁰ Small-scale structure (diameter < 0.6 nm), which is not considered in the model, is another possible source of the deviations.

The distribution function resulting from the fitting procedure for the specimen compacted at 550 °C is plotted in Fig. 3. As noted above, it was assumed that this specimen does not contain significant residual porosity. The curve in Fig. 3, therefore, yields $(1 - q^2)N_1(R)$. The function exhibits a broad distribution in size, ranging from ≈ 3 to ≈ 40 nm. If we assume that the scale of this density fluctuation represents the size of the particles, then a particle diameter of 24.4 nm is deduced. This value is almost twice as large as the average grain diameter determined from the x-ray measurement using the Scherrer equation. We tentatively attribute this difference to the formation of low energy boundaries with high densities. These could form during the initial rapid oxidation treatment, prior to compaction, when the neighboring grains are not constrained from rotating. It would be interesting to learn if the average grain boundary density of nanophase ceramics was indeed a function of the method of synthesis. The rather uncontrolled method of "burning" employed here, unfortunately, is not conducive to such systematic studies.

As a matter of principle, the fraction of interfacial density q , cf. Eq. (3), cannot be separated from the amplitude of the distribution function on the basis of the SANS measurements. However, a relation between volume fraction and interfacial density can be obtained: Integration over the distribution function of Fig. 3 yields,

with consideration of Eq. (5):

$$(1 - q)^2 f_p = 6.6 \times 10^{-2} \quad (7)$$

A second relation between q and f_p can be derived using the macroscopic density of $0.92\rho_0$, where ρ_0 is the rutile density (cf. Table I):

$$f_p \rho_0 + (1 - f_p)q\rho_0 = 0.92\rho_0 \quad (8)$$

In the way Eq. (8) is written, f_p denotes the volume fraction of the bulk rutile grains and $(1 - f_p)$ the fraction of interfacial regions. Combining Eqs. (7) and (8) yields

$$q = 0.70 \quad \text{and} \quad (1 - f_p) = 0.27 \quad (9)$$

which signifies an interfacial density of 70% of the bulk rutile density, covering 27% of the specimen volume. Although these values are reasonable and provide confidence in the assumptions of the model, they can be taken only as crude estimates in view of the uncertainties in the interpretation of $N(R)$ and f_p in a highly dense system where "particles" and "matrix" cannot unambiguously be identified as such.

For the evaluation of the pore contribution to the scattering, it is assumed that the same type of structure as described by $(1 - q^2)N_1(R)$ for the specimen treated at 550 °C is present in all specimens investigated, regardless of their foregoing treatment. The evaluation of the differences then results in the pore volume distributions shown in Fig. 4. The ordinate scale was converted to units of $\text{m}^3/(\text{g}\cdot\text{nm})$ in order to facilitate direct comparison with the BET results shown in Fig. 1.

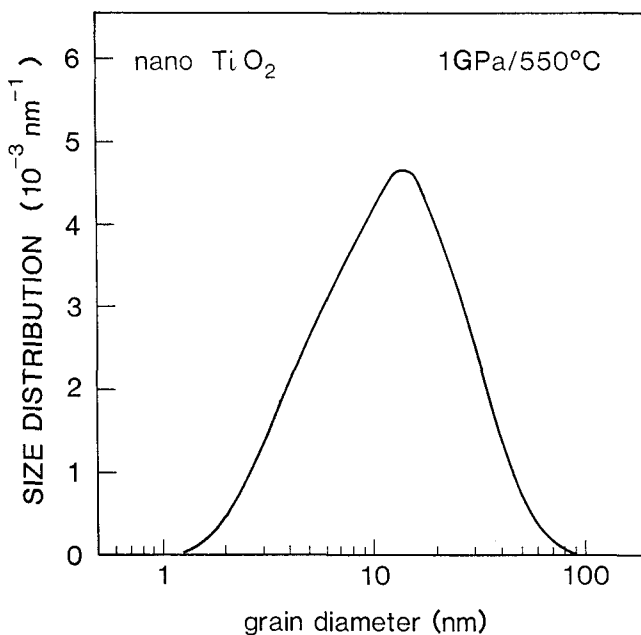


FIG. 3. Size distribution of scattering objects (grains and grain boundaries) in the specimen after compaction at 550 °C, derived from the related SANS results shown in Fig. 2.

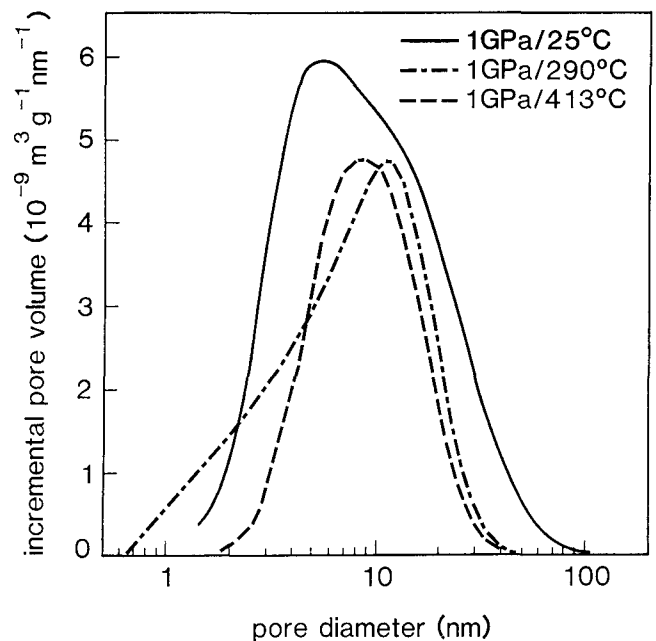


FIG. 4. Pore size distribution in nanocrystalline TiO₂ after compaction at room temperature and at elevated temperatures, as indicated, derived from the related SANS results shown in Fig. 2.

In general, the results of the two techniques are in good quantitative agreement in regards to both the size distribution and the absolute magnitude of $N(R)$. This agreement suggests that both methods, in principle, are suitable for a quantitative analysis of pore size, volume distribution, and volume fraction.

On a finer scale, clear differences are observed between the BET and SANS results. For the specimen compacted at room temperature, a significant volume fraction of pores with diameters between 2 and 8 nm are detected by SANS, but not by BET. Most likely these pores are enclosed and inaccessible to nitrogen adsorption or condensation. A fraction of these small pores survives compaction at 290 °C, but they are completely removed during compaction at 413 °C. The removal of these pores during compaction and sintering at low temperatures is expected since small pores have the highest sintering rates.¹¹

On the large pore-size side of the distribution, a tail in the specimen compacted at 25 °C is detected by both techniques; it extends to about 100 nm in diameter, while the average pore diameter is 21 nm. Compaction at either 290 °C or 413 °C removes a major portion of this coarse porosity, presumably by grain boundary sliding processes that are thermally activated. The pores that survive these compactations have a comparatively narrow size distribution, extending from about 4 to 20 nm in diameter, with the average at 14 nm instead of 21 nm, after the initial preparation.

Table II summarizes the results of average size and pore volume¹² fraction; it also provides a comparison of the different methods applied. The values quantitatively document the above-mentioned similarities and differences. For example, they show that the portion of closed porosity in the sample compacted at room temperature amounts to a volume fraction of about 10%, i.e., one-third of the total porosity. Consequently, the density of this sample is rather less than that deduced from BET and listed in Table I. When the results of SANS and BET are in close agreement, it is evident that the pore structure is open. It signifies that all pores larger than 8 nm in diameter in the as-prepared specimen, and essentially all

pores surviving compaction at 290 °C and 413 °C, are either at the surface or completely interconnected.

V. SUMMARY

In summary, these experiments have demonstrated that SANS can be employed for quantitative measurement of the pore size distribution in ultra-fine-grained ceramic materials and that it provides complementary information to that obtained by BET and gravimetry. An important element in our evaluation of the SANS results, however, was the subtraction of the background scattering from grain boundaries and surface roughness. This was possible in this study by using a reference sample that had a similar grain boundary structure as the test samples, but little residual porosity.

ACKNOWLEDGMENTS

The authors are grateful to H. J. Höfler for help in preparing the specimens and for his comments on the manuscript. The work was supported at The University of Illinois by the United States Department of Energy, Office of Basic Energy Sciences, DEFG02-91ER45439.

REFERENCES

1. R. S. Averback, H. J. Höfler, H. Hahn, and J. C. Logas, *Acta Metall. et Materiala* (in press).
2. H. Hahn, J. Logas, H. J. Höfler, P. Kurath, and R. S. Averback, in *Superplasticity in Metals, Ceramics, and Intermetallics*, edited by M. J. Mayo, M. Kobayoshi, and J. Wadsworth (Mater. Res. Soc. Symp. Proc. **196**, Pittsburgh, PA, 1990), p. 71.
3. H. Karch, R. Birringer, and H. Gleiter, *Nature* **330**, 556 (1987).
4. R. W. Siegel, R. Ramasamy, H. Hahn, Li Zongquan, Lu Ting, and R. Gronsky, *J. Mater. Res.* **3**, 1367 (1988).
5. H. J. Höfler and R. S. Averback, *Scripta Metall. et Materiala* **24**, 2401 (1990).
6. H. Hahn, J. Logas, and R. S. Averback, *J. Mater. Res.* **5**, 609 (1990).
7. G. Kosterz, *Mater. Sci. Forum* **27/28**, 325 (1988).
8. R. Birringer, U. Herr, and H. Gleiter, *Trans. Jpn. Inst. Met.* **27** (suppl.), 43 (1986).
9. K. Ibel, *J. Appl. Cryst.* **9**, 296 (1976).
10. W. Petry, unpublished research.
11. R. J. Brook, *Proc. Brit. Ceram. Soc.* **32**, 7 (1982).
12. The pore volume was deduced from the equation, $0.92\rho_0 \times (1 - f_p) + 0.00\rho_0 f_p = 0.62\rho_0$.

TABLE II. Results on average size (diameter at average volume) of grains and pores and pore volume fraction, derived from BET, SANS, and macroscopic density ρ/ρ_0 , as indicated (specimen denomination as in Table I).

Specimen	Average grain diameter (nm)		Average pore diameter (nm)		Pore volume fraction		
	SANS		BET	SANS	from ρ/ρ_0	BET	SANS
A	14.8		28.4	20.6	0.33	0.19	0.31
B	11.5		11.8	14.0	0.16	0.12	0.17
C	10.6		13.2	13.0	0.13	0.14	0.15
D	12.5		non ^a	non ^a	0 ^a	0 ^a	0 ^a

^aAssumed.